

Wrinkling and Strain Softening in Single-Wall Carbon Nanotube Membranes

E. K. Hobbie,^{1,*} D. O. Simien,² J. A. Fagan,³ J. Y. Huh,³ J. Y. Chung,³ S. D. Hudson,³ J. Obrzut,³
J. F. Douglas,³ and C. M. Stafford³

¹*Department of Physics, Department of Coatings and Polymeric Materials, North Dakota State University, Fargo, North Dakota 58108, USA*

²*Department of Mechanical and Aerospace Engineering, West Virginia University, Morgantown, West Virginia 26506, USA*

³*Polymers Division, National Institute of Standards and Technology, Gaithersburg, Maryland 20899, USA*

(Received 22 December 2009; published 26 March 2010)

The nonlinear elasticity of thin supported membranes assembled from length purified single-wall carbon nanotubes is analyzed through the wrinkling instability that develops under uniaxial compression. In contrast with thin polymer films, pristine nanotube membranes exhibit strong softening under finite strain associated with bond slip and network fracture. We model the response as a shift in percolation threshold generated by strain-induced nanotube alignment in accordance with theoretical predictions.

DOI: [10.1103/PhysRevLett.104.125505](https://doi.org/10.1103/PhysRevLett.104.125505)

PACS numbers: 62.25.-g, 46.32.+x, 61.46.Fg, 68.55.-a

Thin membranes of single-wall carbon nanotubes (SWNTs) show considerable promise for a number of potential applications [1]. The high conductivity and shape anisotropy of the nanotubes enable the formation of conductive quasi-2D networks at remarkably low surface density [2], and the mechanical properties of the individual SWNTs can be outstanding [3]. Recent advances in the separation of SWNTs by length [4] and electronic type [5] allow for the production of membranes with precisely tunable properties, and the tremendous potential of these films for flexible-electronics applications demands a deeper understanding of the coupling between deformation, microstructure, and charge transport. Compressive wrinkling [6,7] has emerged as a powerful tool for engineering [8] and characterizing [9] thin supported films, and we use this approach here to study the nonlinear mechanics of membranes assembled from length purified SWNTs. Our measurements reveal a material that is remarkably stiff under infinitesimal deformation, but which softens dramatically at finite strains. We link this strongly nonlinear behavior to an upward shift in percolation threshold triggered by strain-induced nanotube alignment, an effect correspondingly apparent as an anisotropic decrease in conductivity. Our results are in agreement with theoretical models of percolation in anisotropic rigid-rod networks.

The mechanical characteristics of individual SWNTs can be measured through the amplitude and wavelength associated with periodic buckling under the compressive strain imposed by a flexible polymer substrate [10]. Applying a continuum model to such data yields a SWNT elastic modulus of 1.3 TPa, a remarkable value that accords well with predictions [10]. Analogous mechanical data for SWNT films are limited, however. In one recent study [11], polydisperse chemically functionalized nanotubes were deposited on a stretched polydimethylsiloxane (PDMS) substrate and the mechanics of the cross-linked network queried through the wavelength and

amplitude of wrinkling after release of a single prestrain. Although chemical functionalization is known to have an adverse effect on intrinsic SWNT properties [12], uncross-linked nanotube contacts will be governed by van der Waals attraction, excluded-volume repulsion, and sliding friction [13], raising the possibility of bond slip and network fracture. It is then unclear if the existing theoretical framework, which presumes a homogeneous film with a strain-independent modulus, would be applicable to the pristine SWNT networks of interest here.

Details related to sample preparation, characterization, and analysis can be found in the supporting information [14]. Length-sorted SWNT fractions (>95% purity) with an enrichment in the (6, 5) semiconducting species were prepared from cobalt-molybdenum catalyst (CoMoCat) nanotubes using a dense liquid centrifugation method [4]. The fractions had mean lengths $L = (130, 210, 820, \text{ and } 950) \text{ nm}$ ($\pm 10\%$) with mean diameter $a = 0.75 \text{ nm}$. For each fraction, thin membranes of controlled surface mass density c were prepared by forced filtration of a specific volume of SWNT surfactant solution through acetone-soluble filter paper followed by repeated forced rinsing to remove surfactant. The percolation threshold for each length fraction was determined through impedance spectroscopy [15] and small sections of each membrane were deposited on PDMS by placing them SWNT-face down and dissolving the exposed filter paper with acetone.

The effective film thickness h is a critical parameter and we used atomic-force microscopy (AFM) and near-infrared (NIR) fluorescence microscopy to measure the mean thickness \bar{h} , where $h = \bar{h}/f$ and $f = c/h\rho_s$ denotes SWNT volume fraction in the dry membrane. The measured mean thickness ($10 \text{ nm} < \bar{h} < 100 \text{ nm}$) increased linearly with c independent of L with the inverse slope $\rho_s = (0.7 \pm 0.3) \text{ g/cm}^3$. The structure and topography of the compressed membranes were characterized with reflection optical microscopy, small-angle light scattering

(SALS), AFM, scanning electron microscopy (SEM), and transmission electron microscopy (TEM). For impedance spectroscopy, an aluminum mask was used to deposit two pairs of interdigitated electrodes on the films, one oriented to measure conductivity along the prestrain axis and the other rotated 90° with respect to this. The elastic modulus of the PDMS substrate was measured to be 1.8 MPa. This material is nearly incompressible, and a Poisson ratio of 0.48 was used. The Poisson ratio of SWNT films is reported to be between 0.1 and 0.3 and a value of 0.3 was assumed here [11,16].

A useful point of reference is the continuum model of a thin stiff layer deposited on a much thicker and softer solid that has been stretched to a specified prestrain ϵ [17]. Upon release of the prestrain, a homogeneous film of thickness h and modulus E_f develops a sinusoidal wrinkling pattern of wavelength $\lambda_0 = 2\pi h(\bar{E}_f/3\bar{E}_s)^{1/3}$ and amplitude $A_0 = h\sqrt{\epsilon/\epsilon_c - 1}$ when the ϵ exceeds a critical value $\epsilon_c = \frac{1}{4}(3\bar{E}_s/\bar{E}_f)^{2/3}$, where $\bar{E}_i = E_i/(1 - \nu_i^2)$ is the plane-strain modulus in terms of the elastic modulus E_i and Poisson ratio ν_i of the film ($i = f$) or substrate ($i = s$). At larger strains [17], the substrate is modeled as a neo-Hookean solid and λ_0 is rescaled by a geometrical prefactor to give $\lambda = \lambda_0/(1 + \epsilon)(1 + \xi)^{1/3}$ and $A = A_0\sqrt{1 + \epsilon}/(1 + \epsilon)(1 + \xi)^{1/3}$, where $\xi = 5\epsilon(1 + \epsilon)/32$.

The SWNT films are mesoporous [Fig. 1(b)] with reciprocal-space structure [Fig. 1(c)] that resembles the 2D diffusion-limited aggregation of rodlike particles with long-range attractive interactions [18]. The exponent $D = 1.72$ is insensitive to changes in L and c , consistent with what has been observed in the high-aspect-ratio limit ($L/a \rightarrow \infty$) for the diffusion-limited cluster aggregation of rigid-rod colloids [19]. The primary particle size should have less influence once the nanotubes assemble into a network. Aspect ratio does, however, dictate the percolation threshold, as shown in Fig. 1(d) and as predicted theoretically [15]. Wrinkling does not become apparent until roughly a decade into the regime of electrical percolation. Although rigidity percolation is predicted to emerge at higher densities than connectivity percolation, such differences become relatively small for large aspect ratio [20]. An alternative explanation can be found in the expression for ϵ_c . As shown below, the membrane modulus E_f increases sharply with nanotube area fraction ϕ . This implies a large ϵ_c just beyond the percolation threshold ϕ_c that decreases rapidly with increasing ϕ , and the window of stability reflects the strain interval used in the experiments.

The wrinkling pattern reflects the disordered mesostructure of the membranes, as shown in Fig. 2. In contrast to a pure sinusoid, the deformation is hierarchical with multiple harmonics at progressively smaller length scales [21]. The wrinkle crest of the largest feature contains smaller undulations or folds that can be resolved with AFM and SEM.

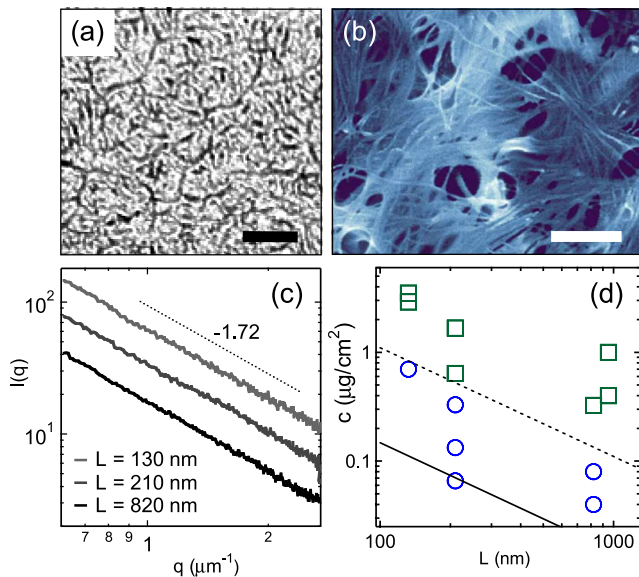


FIG. 1 (color online). (a) Optical micrograph of unstrained membrane ($L = 130$ nm, $c = 3.5 \mu\text{g cm}^{-2}$, scale = $10 \mu\text{m}$). (b) SEM shows a porous assembly of SWNT bundles ($L = 820$ nm, $c = 0.02 \mu\text{g cm}^{-2}$, scale = 200 nm). (c) SALS profiles of unstrained membranes with the exponent D ($L = 130$ nm, $c = 3.5 \mu\text{g cm}^{-2}$; $L = 210$ nm, $c = 1.7 \mu\text{g cm}^{-2}$; $L = 820$ nm, $c = 0.3 \mu\text{g cm}^{-2}$). (d) Wrinkling diagram in the c - L plane. The lower line is the percolation threshold and the upper line denotes the onset of wrinkling (squares).

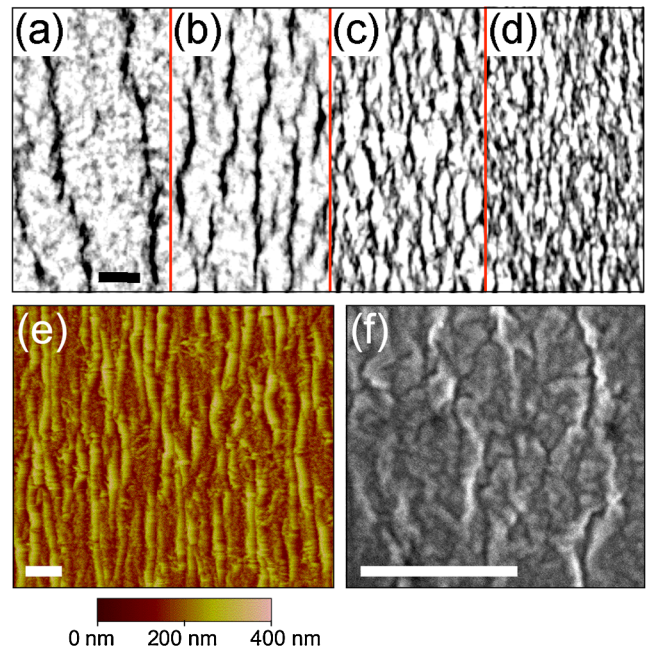


FIG. 2 (color online). Optical micrographs of membrane wrinkling ($L = 130$ nm, $c = 3.5 \mu\text{g cm}^{-2}$) for $\epsilon =$ (a) 2.5%, (b) 5%, (c) 10%, and (d) 20%. (e) AFM and (f) SEM images reveal the complex topography of wrinkling at smaller length scales ($\epsilon = 5\%$). The scale in each image is $5 \mu\text{m}$.

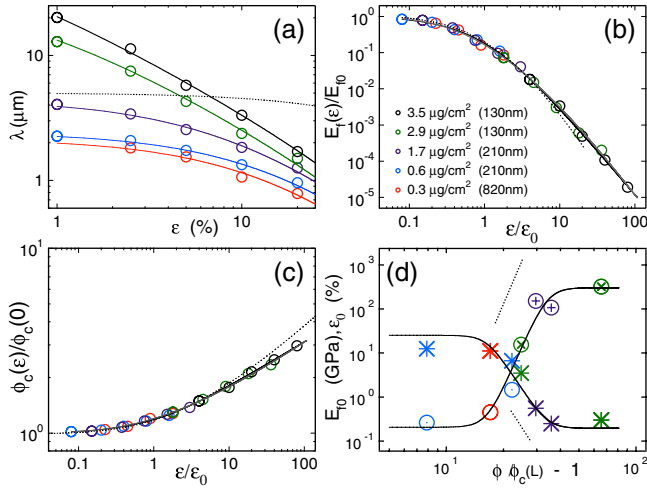


FIG. 3 (color online). (a) Wavelength of the dominant wrinkling mode [legend shown in (b)]. Curves are fits to the strain-softening model derived in the text and the black dashed curve is the nonlinear elastic response [17]. (b) Scaling plot of the softening in E_f , where the black curve is the empirical power-law expression ($\delta = 2.5$) and the dashed ($c_1 = 1.6, w = 1$) and gray ($c_1 = 2.6, w = 0.8$) curves are from Eq. (3). The black and gray curves are nearly indistinguishable. (c) A plot analogous to (b) for the inferred increase in $\phi_c(\epsilon)$. (d) Film modulus (circles) and yield strain (stars) with the suggested power-law behavior; $L = 130$ nm (cross), 210 nm (dot), 820 nm (open), and 950 nm (hatch).

The patterns also contain defect points where the crests merge, bifurcate, or disappear. The dominant wavelength decreases dramatically with ϵ , as indicated in Fig. 3(a). Although the decline is much steeper than predicted by the continuum nonlinear theory, the model can explain these observations if E_f is formally allowed to depend on strain, with the expectation that this softening arises from a progressive strain-induced rupturing of network contacts. The fitted curves in Fig. 3(a) are thus generalizations of the nonlinear model to include $E_f(\epsilon) = E_{f0}(1 + \epsilon/\epsilon_0)^{-\delta}$, where E_{f0} is the modulus with respect to infinitesimal deformation, ϵ_0 is the yield strain, and our data specifically suggest $\delta \approx 2.5$. The softening [Fig. 3(b)] eliminates the usual increase in $A(\epsilon)$ predicted by the continuum model. The wavelength used to extract E_{f0} is an ensemble average over multiple regions of a membrane.

The dramatic increase in modulus with increasing concentration [Fig. 3(d)] and the continuous yielding under finite strain are very reminiscent of behavior observed in sheared 3D carbon-nanotube networks [22–24]. The extracted zero-strain modulus E_{f0} saturates at a value near 250 GPa well below the modulus of an individual SWNT, presumably due to the same dominance of contact forces that arises in concentrated fiber networks [25]. From the exponent D , simple scaling arguments [14] in $d = 2$ give the power-law exponents shown in Fig. 3(d), $E_{f0} \propto [\phi/\phi_c(L) - 1]^\alpha$ and $\epsilon_0 \propto [\phi/\phi_c(L) - 1]^{-\beta}$ with $\alpha = 10$

and $\beta = 6.6$. These independently give $\epsilon_0 \propto E_{f0}^{-2/3}$, suggesting a possible relation between ϵ_0 and ϵ_c . Indeed, inserting the measured film modulus into $\epsilon_c = \frac{1}{4}(3\bar{E}_s/\bar{E}_{f0})^{2/3}$ gives $\epsilon_0 \propto \epsilon_c$ [14], which suggests a single characteristic strain ϵ_c . The data also support L only entering the problem through $\phi_c(L)$, since data for different lengths all fall on the same curve when plotted against $\phi/\phi_c(L) - 1$.

Insight into the exact origin of the softening is provided by the electrical conductivity, which decreases normal to the direction of the prestrain [Fig. 4(a)]. This clearly indicates that conductive pathways are being broken by the anisotropic deformation of the film, presumably the same breakdown of network junctions responsible for softening. We visualize this strain-induced anisotropy directly using TEM. In such images [Fig. 4(b)], the most striking contrast comes from SWNT bundles aligned normal to the strain by the stress imposed on the membrane through the compression and Poisson expansion of the polymer substrate. This alignment is also evident in the structure factor of the membranes measured with SALS [Fig. 4(d)]. The connection between this anisotropy and the decrease in film stiffness and conductivity follows if we consider that the orientation of extended particles reduces the percolation threshold, as recently demonstrated in sheared carbon-nanotube melt composites [26] and stretched SWNT-polymer composites [27].

More quantitatively, the empirical power-law expressions imply a strain dependent percolation threshold $\phi_c(\epsilon)/\phi_{c0} = (1 + \epsilon/\epsilon_0)^\mu$ with $\mu = \delta/\alpha \approx \frac{1}{4}$ [Fig. 3(c)]. We model this using a simplified expression for ϕ_c in anisotropic rigid-rod networks [28];

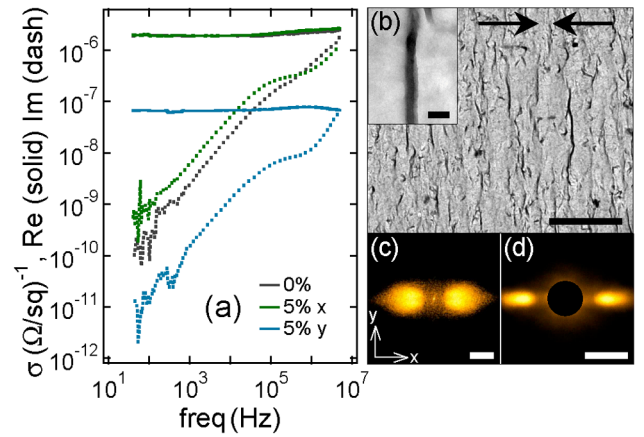


FIG. 4 (color online). (a) Complex conductivity spectra ($L = 130$ nm, $c = 3.5 \mu\text{g cm}^{-2}$), where the black trace is the $\epsilon = 0$ response. A 5% prestrain yields a decrease normal to the prestrain (y), but little change parallel to the prestrain (x). (b) TEM images of the strained membranes show SWNT bundles aligned normal to the prestrain (20% prestrain, $L = 130$ nm, $c = 3.5 \mu\text{g cm}^{-2}$, scale = $5 \mu\text{m}$, and 100 nm for inset). (c) Digital structure factor from an ensemble of optical micrographs and (d) the corresponding SALS pattern (10% prestrain, $L = 130$ nm, $c = 2.9 \mu\text{g cm}^{-2}$, scale = $3 \mu\text{m}^{-1}$).

$$\frac{\phi_c(\epsilon)}{\phi_{c0}} = \left[\frac{5}{\pi} \langle |\sin\theta| \rangle \right]^{-1}, \quad (1)$$

where θ is the orientation angle of a rod with respect to the alignment axis and the brackets denote an average over the orientational distribution function (ODF) $p(\theta)$. An initial approximation for the ODF [14] that neglects rod-rod interactions, and thus underestimates anisotropy, follows from the relaxation of the PDMS, $p(\theta) \propto [(1 + \epsilon)^2 \sin^2\theta / (1 - \nu_s \epsilon)^2 + \cos^2\theta]^{-1}$. Defining the 2D orientational order parameter $S = 2\langle \cos^2\theta \rangle - 1$, this ODF gives $S = 0.14$ at $\epsilon = 20\%$. To include interactions and account for yielding, we generalize this to

$$p(\theta) \propto \frac{1}{(1 + c_1 \epsilon / \epsilon_0)^w \sin^2\theta + \cos^2\theta}, \quad (2)$$

with fitting parameters c_1 and w , which has the correct $\epsilon \rightarrow 0$ limit. This gives

$$\frac{\phi_c(\epsilon)}{\phi_{c0}} = \left(\frac{\pi^2}{10} \right) \frac{\sqrt{(1 + c_1 z)^w - 1}}{\tanh^{-1} \sqrt{1 - (1 + c_1 z)^{-w}}} \quad (3)$$

and

$$S = \frac{(1 + c_1 z)^{w/2} - 1}{(1 + c_1 z)^{w/2} + 1}, \quad (4)$$

where $z = \epsilon / \epsilon_0$. The dashed curves in Figs. 3(b) and 3(c) follow from Eq. (3) with $c_1 = 1.6$ and $w = 1$ ($S = 0.7$ at $z = 20$) and the gray curves in Figs. 3(b) and 3(c) correspond to $c_1 = 2.6$ and $w = 0.8$ ($S = 0.65$ at $z = 20$). A comparison of Figs. 4(c) and 4(d) suggests that the anisotropy in the microstructure is greater than that in the wrinkling pattern, the SALS data being consistent with the fitting results $c_1 = 2.6$ and $w = 0.8$.

A remarkable aspect of these films is the degree of microscale anisotropy that develops under modest strain. As noted above, a dilute SWNT coating would be anticipated to exhibit $S = 0.14$ at $\epsilon = 20\%$, but both the TEM and SALS data suggest much stronger anisotropy than this. The films in question have effective SWNT volume fractions approaching 0.5, where the combined effects of excluded volume and attractive van der Waals interactions will favor a closely packed arrangement of aligned nanotubes in response to a weak perturbation. Such regions are directly revealed by TEM [Fig. 4(b)]. Although this alignment is irreversible, there is a surprising degree of reversibility at small strains [14]. Somewhat analogous behavior is observed in stretched collagen gels, which strain harden through irreversible fiber alignment in the absence of physical crosslinks [29].

Our generalization of the nonlinear continuum model to films with a strain dependent modulus is successful in capturing essential aspects of wrinkling in SWNT membranes, and simple scaling arguments can account for changes in film mechanical properties with concentration and stress. The hypothesis of network destruction due to

nanotube alignment has been independently confirmed through conductivity measurements, and is very reminiscent of the type of strain-softening behavior exhibited by a broad class of polymer-nanocomposite systems. Applications that require flexible SWNT coatings will seek to exploit the window of stability in Fig. 1(d), where conductive films can accommodate up to 20% strain without wrinkling. The measurements and analysis presented here should help guide the production of such films. A greater challenge will be engineering membranes that wrinkle reversibly without chemical crosslinking, perhaps through the introduction of a second interpenetrating polymer network.

*Corresponding author.
erik.hobbie@ndsu.edu

- [1] Q. Cao and J. A. Rogers, *Adv. Mater.* **21**, 29 (2009).
- [2] Z. Wu *et al.*, *Science* **305**, 1273 (2004).
- [3] A. Kis and A. Zettl, *Phil. Trans. R. Soc. A* **366**, 1591 (2008).
- [4] J. A. Fagan *et al.*, *Adv. Mater.* **20**, 1609 (2008); J. A. Fagan *et al.*, *Langmuir* **24**, 13880 (2008).
- [5] M. S. Arnold *et al.*, *Nature Nanotech.* **1**, 60 (2006); M. C. Hersam, *Nature Nanotech.* **3**, 387 (2008).
- [6] E. Cerda and L. Mahadevan, *Phys. Rev. Lett.* **90**, 074302 (2003).
- [7] L. Pocivavsek *et al.*, *Science* **320**, 912 (2008).
- [8] C. J. Rand *et al.*, *Soft Matter* **4**, 1805 (2008).
- [9] C. M. Stafford *et al.*, *Nature Mater.* **3**, 545 (2004).
- [10] D.-Y. Khang *et al.*, *Nano Lett.* **8**, 124 (2008).
- [11] C. Yu *et al.*, *Adv. Mater.* **21**, 4793 (2009).
- [12] C. Wang *et al.*, *J. Am. Chem. Soc.* **127**, 11460 (2005).
- [13] M. Lucas *et al.*, *Nature Mater.* **8**, 876 (2009).
- [14] See supplementary material at <http://link.aps.org/supplemental/10.1103/PhysRevLett.104.125505> for details.
- [15] D. Simien *et al.*, *ACS Nano* **2**, 1879 (2008).
- [16] L. J. Hall *et al.*, *Science* **320**, 504 (2008).
- [17] H. Jiang *et al.*, *Proc. Natl. Acad. Sci. U.S.A.* **104**, 15607 (2007).
- [18] A. Vincze *et al.*, *J. Phys. Chem. B* **106**, 2404 (2002).
- [19] A. Mohraz *et al.*, *Phys. Rev. Lett.* **92**, 155503 (2004).
- [20] M. Latva-Kokko and J. Timonen, *Phys. Rev. E* **64**, 066117 (2001).
- [21] K. Efimenko *et al.*, *Nature Mater.* **4**, 293 (2005).
- [22] E. K. Hobbie and D. J. Fry, *Phys. Rev. Lett.* **97**, 036101 (2006).
- [23] S. B. Kharchenko *et al.*, *Nature Mater.* **3**, 564 (2004).
- [24] L. A. Hough *et al.*, *Phys. Rev. Lett.* **93**, 168102 (2004).
- [25] M. Alava and K. Niskanen, *Rep. Prog. Phys.* **69**, 669 (2006).
- [26] J. Obrzut *et al.*, *Phys. Rev. B* **76**, 195420 (2007).
- [27] S. I. White *et al.*, *Phys. Rev. B* **79**, 024301 (2009).
- [28] I. Balberg *et al.*, *Phys. Rev. B* **30**, 3933 (1984).
- [29] D. Vader, A. Kabla, D. Weitz, and L. Mahadevan, *PLoS ONE* **4**, e5902 (2009).